LRP 769/03 August 2003

Papers presented at the 15th Topical Conference on Radio Frequency Power Plasmas

Moran, Wyoming, U.S.A.,
May 19 - 21, 2003

To appear in
AIP Conference Proceedings

ISSN 0458-5895

LIST OF CONTENTS Page

Physics Studies with ECH/CD in the TCV Tokamak

A.Pochelon, S.Alberti, C.Angioni, G.Arnoux, R.Behn, P.Blanchard, Y.Camenen, S.Coda, I.Condrea, T.P.Goodman, J.Graves, M.A.Henderson, J-Ph.Hogge, E.Nelson-Melby, P.Nikkola, L.Porte, O.Sauter, A.Scarabosio, M.Q.Tran, G.Zhuang, TCV Team

Centre de Recherches en Physique des Plasmas CRPP EPFL, Association EURATOM-Confédération Suisse, Ecole Polytechnique Fédérale de Lausanne EPFL, CH-1015 Lausanne, Switzerland

Abstract. The TCV tokamak program is centred on flexible plasma shaping matched by a flexible auxiliary-heating system based entirely on ECH at 2nd and 3rd harmonics. This paper reviews some of the recent highlights of TCV ECW (Electron Cyclotron Waves) results. Very high elongation high q plasmas, which would be vertically unstable in Ohmic conditions, are stabilised by broadening the current profile making use of far off-axis ECH or ECCD. Central power deposition in such a configuration can be achieved at high central density (beyond 2nd harmonic cut-off) using 3rd harmonic heating. The 3rd harmonic power deposition meets expectations with coupling of up to 100% and feedback is developed to maximise coupling in transient conditions. Experimental measurements and Fokker-Planck modelling suggest that radial diffusion of suprathermal electrons play a crucial role in determining the ECCD efficiency at the maximum EC power density of TCV. Fully sustained off-axis ECCD scenarios have allowed the creation of plasmas with broad steady-state electron ITBs, high bootstrap fractions (80%) and reversed central shear. Reversed central shear and eITBs have also been developed in discharges dominated by inductive current by combining off-axis heating with central counter CD. Shortening of sawtooth period, useful in NTM avoidance schemes, is produced with local power deposition just inside the q=1 surface.

1. INTRODUCTION

An essential part of the TCV tokamak program is dedicated to the study of the effect of plasma shape on plasma confinement and stability. ECW, offering power coupling independent of the plasma-launcher distance, was an obvious choice. Moreover, the most important property that ECWs offer is localised power deposition in real space and phase space, a crucial property for the control of instabilities (sawtooth or NTM), or for the control of the current profile (enhanced confinement or vertical stability).

The TCV ECW system is composed of six 2nd harmonic X2 gyrotrons and LFS launchers (3MW, 2s, 82.7GHz, $n_{e\ \text{cut-off X2}} = 4.3\times10^{19}\text{m}^{-3}$) and three 3rd harmonic X3 gyrotrons using one top launcher (1.5MW, 2s, 118GHz, $n_{e\ \text{cut-off X3}} = 11.5\times10^{19}\text{m}^{-3}$). All launchers have two degrees of freedom and can be steered in real time [1]. This represents high power density with potentially more than 30MW/m^3 in central X2 injection. The relative alignment of the different launcher mirrors is accomplished using the highly localised sawtooth period response at the q=1 resonant surface. The main codes used are TORAY-GA for the ray tracing and linear CD [2], Fokker-Planck CQL3D (X2&X3) with hard X-ray module [3], equilibrium LIUQE and CHEASE [4] and transport PRETOR [5] including also sawtooth stability, PRETOR-ST [6].

2. CURRENT PROFILE BROADENING WITH OFF-AXIS ECW

Vertical stability of high elongation κ plasmas requires broad current profile $j(\rho)$, as in Ohmic low-q high-current discharges. High κ operation has been extended to lower currents at constant quadrupole field using far off-axis ECW to broaden the current profile, thereby creating high κ discharges that would otherwise be ohmically unstable [7], as shown in Fig. 1a. This enables us to study the stability and confinement properties of a wider range of elongations and current profiles. The current profile broadens on a resistive time scale through T_e-profile broadening, which is caused by an ECH deposition at ρ_{dep}~0.5-0.7, as shown in the discharge evolution of phase 1 of Fig. 1b. The radial co-ordinate used is $\rho=(V/V_{LCFS})^{1/2}$, where V is the volume inside the flux surface considered.

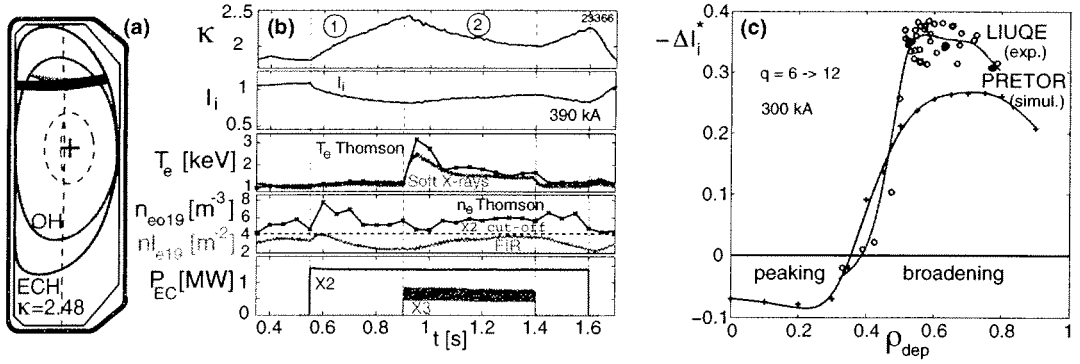

FIGURE 1. a) Increase of elongation using far off-axis ECH deposition, **b)** Parameter evolution in a discharge first elongated with far off-axis X2 (phase 1), then centrally heated with X3 (phase 2, see section 3). **c)** Δl_i vs ρ_{dep}, showing the narrow layer of effective j-broadening.

The change in amplitude of l_i (and κ) depends strongly on the deposition location [8], as shown in Fig. 1c. Modifications are very effective in a narrow radial layer, typically $0.55<\rho_{dep}<0.7$. Inside a pivot point at $\rho_{dep}=0.4$ the deposition generates current peaking. This pivot point moves to a larger radius for higher plasma current, pushing the effective layer further out. These results are confirmed by PRETOR transport code simulations. Increasing the power deposited off-axis increases the broadening effect. At higher power, it increases less, which suggests an increase of the thermal diffusivity χ_e outside ρ_{dep} with absorbed power, and is again confirmed by PRETOR transport simulations. Injecting the EC beam at a toroidal angle of typically $\varphi=\pm15^\circ$ appreciably improves effectiveness by 15-20% over ECH conditions ($\varphi=0^\circ$). The improvement is not due to ECCD since injection occurs totally in the trapped electron region of phase space as demonstrated by CQL3D calculations, but is due to the fast electrons generated, effectively measured on the HFS ECE diagnostics, and decreasing the loop voltage symmetrically for both $\varphi=\pm15^\circ$.

Operation of X2 at high-density, even at densities above cut-off in the core, improves current profile broadening effectiveness. This is both due to the usual improvement of electron confinement time with density, which is reflected by a large reduction of χ_e outside the deposition location, and by the increased P_{ei} transfer in the core due to peaked density profiles, flattening the central T_e-profile measured from Thomson scattering. The presence of high harmonics MHD modes with $q=m/n=1$ (1/1, 2/2, 3/3) measured from a 64-channel multi-wire proportional soft X-ray camera [9] is also indicative of a flatter central current profile [10]. At high-density (n_{eo}~6×10^{19}m^{-3}), 1MW was sufficient to raise the elongation from 1.7 to 2.5 at 300kA, using the narrow deposition layer for effective current profile broadening.

3. CENTRAL X3 HEATING IN ELONGATED PLASMAS

Third harmonic X3 heating is exploited for central heating in conditions overdense to X2. Taking the above elongated discharges as an example, X3 power absorption is maximised by launching the wave from the top with a shallow incidence of the beam on the resonance layer, Fig. 2 [11]. Here, the X3 launching mirror angle was optimised to maximise the electron temperature T_{eo} rise soon after the start of X3 (t=0.95s) since the density and equilibrium transients did not allow optimisation of performance throughout the discharge, see phase 2 of Fig. 1b. With far off-axis deposition, X2 can be operated with a central density up to typically twice X2 cut-off density, (i.e. half to two-thirds X3 cut-off density) [7], with significant refraction of X2 and X3 beam paths (Fig. 2). The central region in cut-off of X2 is indicated.

When X3 heating is applied, the elongation starts to decrease due to X3 central power deposition peaking the current profile. The rigid body growth rate γ_{RB} of the vertical instability during X2 increases with elongation (initial phase 1), but starts to decrease at the onset of X3, probably due to a predominance of the decrease of κ over the peaking of $j(\rho)$. Efforts at maintaining constant high elongation during X3 heating by increasing the equilibrium quadrupole field, otherwise maintained constant in these experiments, leads to loss of vertical equilibrium, unless X2 far off-axis power deposition is increased to oppose the X3 current peaking effect.

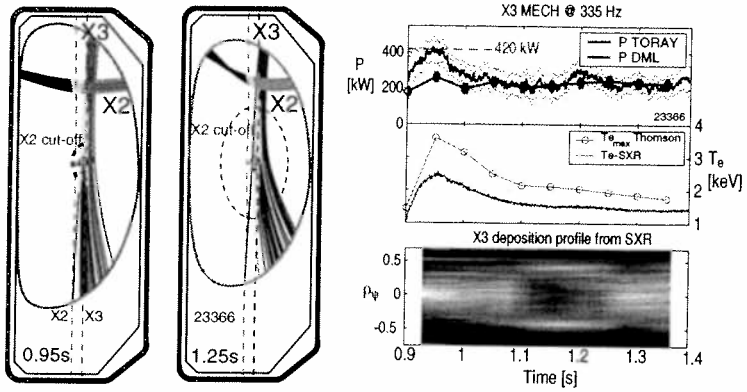

FIGURE 2. Central X3 heating on X2 far off-axis elongated plasma at two different times; the position of the cold resonances and cut-offs are indicated.

FIGURE 3. X3 modulated ECH DML power compared with power absorbed from ray tracing, central temperature evolution from Thomson and soft X-rays absorber method, power deposition profile from soft X-rays.

The total X3 power coupled and its deposition profile are measured by modulation techniques [12]. The time evolution of the measured and predicted X3 absorbed power (from diamagnetic loop (P_{DML}) and ray tracing TORAY-GA (P_{TORAY}), respectively), the central electron temperature (by Thomson and soft X-ray), and the emissivity profile measured with a 64 channel soft X-ray wire chamber (MPX) are shown in Fig. 3. Both the DML and MPX yield reliable results with a response phase close to 90° at an optimal X3 power modulation frequency (337Hz). The power deduced from the DML is identical to that from ray tracing for most of the time slices, which implies a fully thermal plasma. For these times the deposition profile, similar to the one deduced from ray tracing, is monotonic and peaked on axis. The fact that $P_{DML}>P_{TORAY}$ indicates absorption on suprathermal electrons. The presence of suprathermal electrons is confirmed by $T_{ECE}/T_{Thomson}>1$, where T_{ECE} is the radiation temperature measured with a high-field side radiometer. The suprathermal electrons

are created during the X2 phase ($\varphi \neq 0^{o}$) and persist over most of the X3 heating phase. At the beginning of X3, full absorption is measured by the DML, the power being shared between bulk and suprathermal absorption, since this full absorption is correlated with an increase of the T_{ECE}-profile (with $T_{rad} > T_{Thomson}$).

4. X3 POWER DEPOSITION AND ABSORPTION

The experiments described in section 3 confirm that X3 absorption is very sensitive to X3 launcher angle. The assessment of X3 heating and power deposition is made in more steady-state plasmas [13]. An example of a top launcher angle sweep during a medium density discharge is shown in Fig. 4a. The plasma soft X-ray response and the absorption calculation from ray tracing are compared, Fig. 4b. For all densities up to 3/4 of cut-off density, there is good overlap showing that ray tracing appears adequate to describe the absorption. It shows that differences of the order of 0.2^{o} in the mirror angle, or variations of the plasma parameters can significantly modify the absorbed power, motivating the development of a feedback system to maximise absorption throughout the discharge.

Experiments were performed to test real-time data analysis methods and to determine the best signal for use in real-time feedback control of the launching mirror angle. In these experiments the launcher mirror angle was swept linearly in time through the resonance layer with a low amplitude sinusoidal oscillation superimposed. The oscillation allows us to determine the maximum response by examining the phase and amplitude of the perturbations measured on a soft X-ray camera with a line of sight through the plasma centre. Figure 5 shows the applied perturbation and the plasma response, as well as the amplitude and phase of the analysed signals [14]. Using the phase response as a feedback signal it will be possible to adjust the launcher angle in real time to maintain maximum absorption throughout the discharge. Algorithms that can be implemented in a digital signal processing system are being developed.

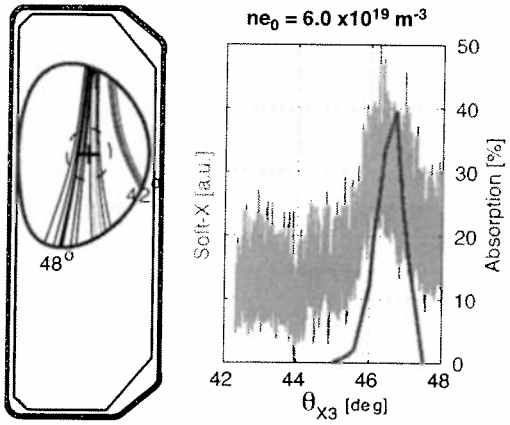

FIGURE 4. X3 mirror angle sweep:
a) X3 mirror angles θ_{X3} of Fig. 4b),
b) soft X-ray plasma response and TORAY absorbed power fraction.

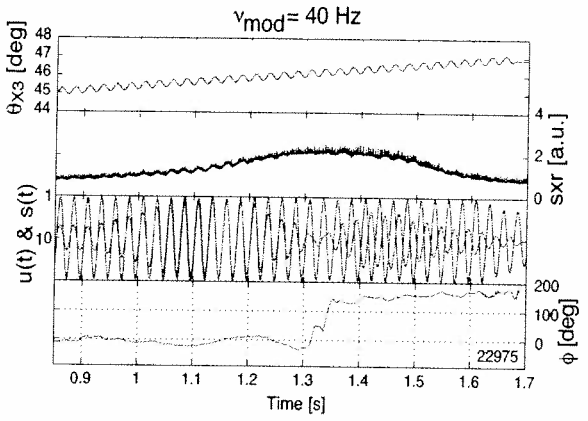

FIGURE 5. X3 mirror angle sweep with a 40Hz dithering, soft X-ray response, phases of soft X-ray and mirror angle, phase difference exhibiting a phase jump at maximum coupling location.

5. SUPRATHERMAL ELECTRON TRANSPORT WITH STRONG ECCD

Steady-state fully sustained ECCD discharges are used for the study of ECCD efficiency in the absence of any inductive component ($E_{||}$=0). At the high power densities in TCV (even >30MW/m^3), non-linear effects in Fokker-Planck calculations were predicted to enhance markedly current drive efficiencies above normalised power densities of Q_e[MW/m^3]/n_e^2[10^{19}m^{-3}] ~ 0.5 [15]. However, with normalised power densities in excess of 10 in the same units, non-linear effects were not observed as strong as predicted, requiring a better understanding of suprathermal electron transport. A hard X-ray camera (15 spatial chords each with 8 energy bins between 10 and 100keV [16]) and a HFS ECE [17] radiometer provide fast electron measurements. The hard X-ray emission profiles after inversion show an emission going from peaked to hollow when the deposition is moved from the core to edge, but are always broader than the ECCD calculated deposition location, Fig. 6a, thus providing a first evidence of radial transport [18]. The time delay of the ECE response to an ECCD pulse increases with distance from deposition, Fig. 6b, a second evidence of transport.

The hard X-ray emissivity spectrum along different plasma chords was simulated with CQL3D with a central fast electron diffusivity 1.5<D_o<5m^2/s, Fig. 7 (loop voltage V_l≠0, central co-CD deposition ρ_{co}~0.2, L-mode plasma). The diffusion coefficient was chosen to match the observed to the simulated I_p-I_{BS} value, where the bootstrap current is obtained from Thomson electron pressure profiles. The simulation of the photon temperature yields a flat radial profile in agreement with experiment [19], whereas zero diffusion would yield a photon temperature peaked on axis. In fully ECCD sustained discharges, matching I_{CD}=I_{tot}-I_{BS} with the simulated driven current $I_{CD\text{-}FP}$ yields both the diffusivity, 0.5<D_o<1 m^2/s, and the driven current profile $j(\rho)$, Fig. 8 (V_l=0, ρ_{co}~0.45, eITB plasma). The results are fairly independent of the transport model used [20].

The simulated $I_{CD\text{-}FP}$ without diffusion can easily be ten times higher than with the diffusivity suggested by suprathermal electron measurements, and a deposition off-axis can generate current deposition profiles peaked on-axis. The non-linear current drive enhancement is strongly reduced by such high suprathermal electron diffusion at these high power densities, but it still increases the CD efficiency above the linear efficiency at the power level used.

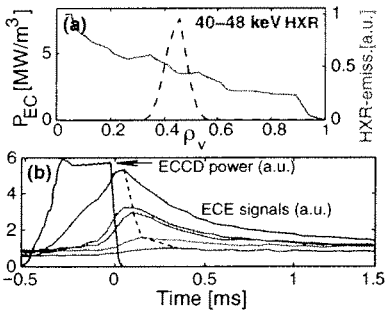

FIGURE 6. Evidence of suprathermal diffusion, **a)** local deposition leads to delocalised hard X-ray emission, **b)** HFS ECE signals indicating time delays increasing with distance to ECCD pulse.

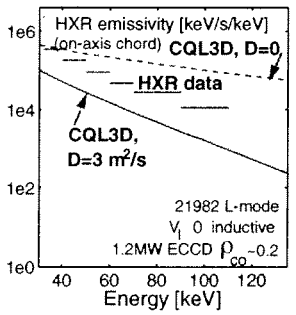

FIGURE 7. Measured and simulated hard X-ray spectra for a central co-ECCD power deposition.

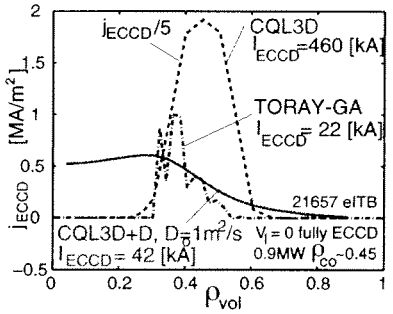

FIGURE 8. Driven current from TORAY (linear), CQL3D (quasi-linear) with and without radial diffusion. Both the I_{CD} value and j-profiles are strongly affected by radial diffusion.

6. FULLY SUSTAINED ECCD SCENARIOS WITH EITBs

Different ECW scenarios are used to form electron internal transport barriers (eITBs) in fully ECCD sustained discharges [21]. The eITBs are formed in the current plateau, without exploiting the help of the strong current rise and with no momentum input. The standard schemes used are: 1) co-ECCD deposited off-axis with ECH on-axis to obtain fully ECCD sustained discharges, 2) ECH off-axis with counter on-axis to form eITBs in inductive discharges [22].

The first approach is described here. The eITB develops with co-ECCD applied off-axis at $\rho_{co} \geq 0.35$ (0.9MW) and typically with ECH on-axis (0.45MW) with $V_l=0$ set by I_{OH}=const., I_p=90kA, $n_{eo}=10^{19}m^{-3}$, κ=1.55, δ=0.5. Co-ECCD broadens the current and pressure profiles. The pressure gradient steepens, which increases the bootstrap current fraction I_{BS}/I_{tot}. A hollow total current density profile j_{tot} develops on a few current redistribution times τ_{CR} with non-monotonic q-profile, carried by j_{BS}, since the j_{CD} is rather flat (see section 5). The addition of central ECH or counter-CD enhances the pressure gradient increasing the bootstrap fraction, increasing the reverse shear, Fig. 9a, and enhancing the barrier performance. This is confirmed by an increase of τ_{Ee} with increased central power deposition.

Displacing ρ_{co} outwards improves the confinement $H_{RLW}=\tau_E/\tau_{RLW}$ for $\rho_{co}>0.35$, Fig. 9b. The increase of confinement is associated with an enlargement of the high confinement volume which scales as $\rho^2_{q\text{-}min}$ and ρ^2_{eITB} [23] (defined as the location $\rho_{\rho*}$ of the maximum of $\rho^*_T(\rho) \equiv \rho^*_{Tmax}$) [24]. Giving a toroidal angle on the central ECH beam, $\varphi=0^o$, to launch counter-CD (co), while maintaining the same deposition for the off-axis co-ECCD, further enhances (degrades) the confinement, Fig. 9c. The counter-CD creates a hollower current profile, which enhances the eITB. The confinement enhancement is attributed to a more reversed shear with q_o/q_{min} and ρ^*_{Tmax} increasing.

The confinement enhancement at the eITB can be controlled either by increasing the volume enclosed by the barrier (ρ^2_{eITB} or $\rho^2_{q\text{-}min}$) by increasing the off-axis co-EC-CD deposition radius, or by increasing the shear reversal factor q_o/q_{min} or ρ^*_{Tmax} with on-axis counter-CD. The global figure of merit for the eITB can be expressed as $H_{RLW} \sim q_o/q_{min} \times \rho^2_{q\text{-}min}$ [23] or with Thomson data, $H_{RLW} \sim \rho^*_{Tmax} \times \rho^2_{eITB}$, Fig. 9d [25].

In inductive discharges, with ECH deposition off-axis, increasing the power of counter-CD in the core is another way to create reverse shear and enlarge $\rho_{q\text{-}min}$ and ρ_{eITB}. This scenario ($P_{ECH\_off\text{-}axis}$=0.9MW and $P_{counter\text{-}CD\_central}$=1.35MW) allowed the achievement of record electron temperatures of 15-18keV, with β_N close to 1.5.

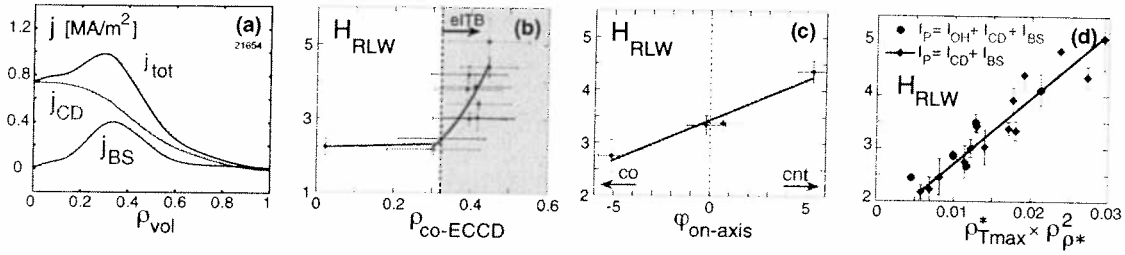

FIGURE 9. eITBs in fully sustained ECCD discharges: **a)** off-axis co-CD deposition at ρ=0.4 leads to non-monotonic $j(\rho)$. The hollow total current j_{tot} is due to the bootstrap current. Improvements of H_{RLW} achieved by **b)** displacing $\rho_{co}>0.3$, **c)** changing central ECH to counter-CD; **d)** confinement enhancement scales with the barrier strength × barrier volume, i.e. $\rho^*_{Tmax} \times \rho^2_{eITB}$ (also some inductive data).

7. SAWTOOTH CONTROL WITH LOCALISED POWER DEPOSITION

Large sawteeth can seed NTMs, reducing their onset β_N [26]. Shortening the sawtooth period (destabilising sawteeth) by means of adequate local power deposition is therefore of interest. Recent sawtooth control experiments with ECW [6] have been undertaken in several machines, also in the presence of ion heating [27]. Sawtooth period maximisation using a poloidal mirror sweep through the location of the q=1 surface ρ_1 has been regularly used as the most efficient means of cross-calibrating the alignment of the different launchers, to an accuracy of 2% radius (~5mm). The sawtooth period is a nearly linear function of the power density [28, 29, 6], thereby allowing also an alternate measurement of the beam width [29]. The sawtooth period response to localised deposition can be simulated with the PRETOR-ST [6] code. For destabilisation, that is to make the q=1 shear $s_1=dq_1/dr$ steeper, both heating and co-CD inside ρ_1, or counter-CD outside ρ_1 can be used. For stabilisation, that is to flatten s_1, both heating and co-CD outside ρ_1, or counter-CD inside ρ_1 can be used [6].

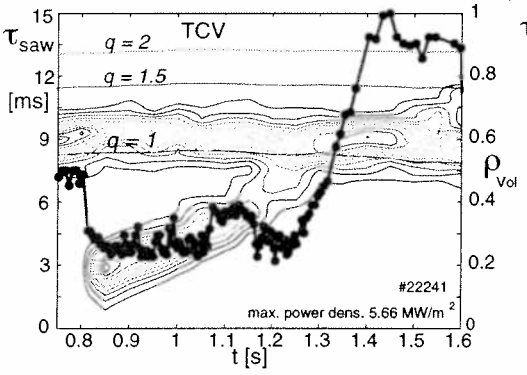

FIGURE 10. Experimental sawtooth period, position of main rational q-surfaces (LIUQE) and TORAY-GA ECH power density contours: 0.9MW ECH (slight co-CD) placed for optimal stabilisation; 0.45MW of swept ECH (slight co-CD). Localised heating is found to destabilise sawteeth inside q=1.

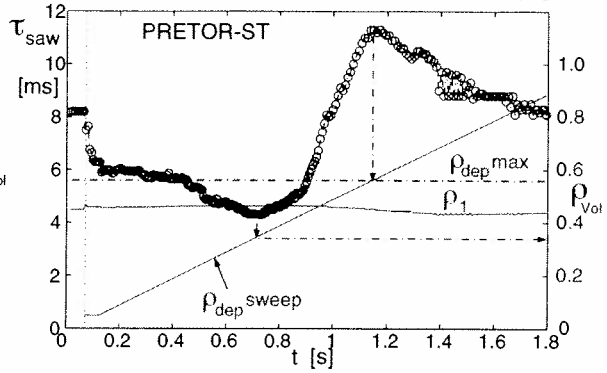

FIGURE 11. Simulated sawtooth period in the case of a full radial sweep of localised 0.45MW of ECH, while stabilising sawteeth with 1.35MW at the fixed ρ_{max}.

A case with multiple beams and high total power is shown for illustration. Several beams (2 in the experiment, Fig. 10, and 3 in the predictive simulation, Fig. 11) deposit the power at the location maximising the sawtooth period, ρ_{max}, (ρ_{dep}~0.6). Another single beam sweeps the power deposition from the plasma centre to the edge. The stabilising power deposited beforehand at ρ_{max} increases the sensitivity of the destabilising effect of the swept beam. In the present case, both experiment and simulation yield optimal stabilisation for ρ_{max}/ρ_1~1.2-1.3. Simulations show that the location of most efficient sawtooth stabilisation depends on the deposition width $\Delta\rho$, such that $\rho_{max}\sim\rho_1+\Delta\rho/2$. Since the stabilisation/destabilisation effect is proportional to the power density, this confirms the advantage of narrow and intense power deposition offered by ECW techniques. Optimal destabilisation is obtained for a deposition totally inside ρ_1 with discrepancies between simulation and experiment presumably due to finite-island size. Figures 10 and 11 provide evidence that modelling of sawteeth is in close agreement with experiment.

8. CONCLUSIONS

High power far off-axis locally deposited X2 ECW allows broad current profiles and improved vertical stability. At the maximum ECCD power densities in TCV, suprathermal diffusion, assessed by hard X-ray and HFS ECE measurements, plays a central role in the resulting ECCD efficiency and radial j_{CD} profile. The local deposition of co-, counter-ECCD and ECH powers are used as tools to shape eITB in fully ECCD sustained discharges and inductive discharges, making TCV an ideal resource for various current profile tailoring experiments. Sawtooth control is more effective with high power density and sawtooth destabilisation is obtained with deposition inside q=1. Initial X3 heating has demonstrated full power absorption in high-elongation high-density discharges. The X3 launcher feedback is being developed to couple efficiently during evolving target plasmas.

ACKNOWLEDGMENTS

The authors recognise the competent support of the entire TCV team. This work was partly supported by the Swiss National Science Foundation.

REFERENCES

1. Goodman T.P. et al., *Proc. of the 19th Symposium on Fusion Technology*, Lisbon, (1996) 565.
2. Matsuda, K., *IEEE Transactions on Plasma Science* **PS-17** (1989) 6.
3. Harvey, R.W., et al., *Proc. of the IAEA Tech. Conf. on Advances in Simulation and Modelling of Thermonuclear Plasmas*, Montreal, 1992, (IAEA, Vienna, 1992).
4. Lütjens H., Bondeson A., Sauter O., *Computer Physics Communications*, **97** (1996) 219.
5. Boucher D., Rebut P.-H., *Proc. of the IAEA Tech. Conf. on Advances in Simulation and Modelling of Thermonuclear Plasmas*, Montreal, 1992, (IAEA, Vienna, 1992) 142.
6. Angioni C., et al., *Nuclear Fusion* **43** (2003) 455.
7. Pochelon A., et al., *19th IAEA Fusion Energy Conf.*, Lyon 2002, France, IAEA-CN-94/EX/P-14.
8. Camenen Y. et al., *Proc. of 12th Joint Workshop on ECE and ECRH (EC-12)*, Aix-en-Provence 2002, (World Scientific, Singapore, 2002) 407.
9. Sushkov A. et al, *29th EPS Conf. on Plasma Phys. and Contr. Fusion*, Montreux 2002, ECA Vol. **26B** (2002) Paper P4-118.
10. Duperrex P.-A., Pochelon A., et al., *Nuclear Fusion* **32** (1992) 1161.
11. Hogge J.-P., et al., *EC-12*, Aix-en-Provence 2002, p. 371, accepted for publ. in Nuclear Fusion.
12. Manini A., Moret J.-M., et al., *Plasma Phys. Control. Fusion* **44** (2002) 139.
13. Alberti S., et al., *29th EPS*, Montreux 2002, ECA Vol. 26B (2002), Paper P0-273.
14. Porte L., et al., *19th IAEA Fusion Energy Conference*, Lyon 2002, France, IAEA-CN-94/EX/P5-15.
15. Harvey R.W., *Physical Review Letters* **62** (1989) 426.
16. Peysson Y., Coda S. Imbeaux F., *Nucl. Instrum. and Methods in Phys. Res. A* **458** (2001) 269.
17. Blanchard, P., et al., *Plasma Phys. Control. Fusion* **44** (2002) 2231.
18. Coda S., et al., *19th IAEA FEC*, Lyon 2002, France, IAEA-CN-94/EX-W5, to appear in NF.
19. Harvey, R.W., Sauter O., Prater R., Nikkola P., et al., *Physical Review Letters* **88** (2002) 205001.
20. Nikkola, P., et al., to be publ. in *Nucl. Fus.*; *EC-12*, Aix-en-Provence (2002) 257.
21. Sauter O., et al., *19th IAEA FEC*, Oct. 2002, Lyon, France, IAEA-CN-94/EX/P5-06.
22. Behn R., et al., *30th EPS Conf. on Plasma Phys. and Contr. Fusion*, St. Petersburg 2003.
23. Henderson M., et al., *44th APS Plasma Div.*, Orlando 2002, to be publ. in *Phys. of Plasmas*, 2003.
24. Tresset G., Litaudon X., Moreau D., Garbet X., et al., *Nuclear Fusion* **42** (2002) 520.
25. Martin Y., et al., *30th EPS Conf. on Plasma Phys. and Contr. Fusion*, St. Petersburg 2003.
26. Sauter O., Westerhof E., Mayoral M.L., et al., *Phys. Rev. Lett.* **88** (2002) 105001.
27. Goodman T., Mück A. et al., *19th IAEA-FEC*, Lyon 2002, France, IAEA-CN-94/EX/P5-11.
28. Goodman T.P. et al, *26th EPS*, Maastricht 1999, ECA Vol. 23J (1999), 1101.
29. Henderson M.A., Goodman T.P., et al., *Fusion Engineering and Design*, **53** (2001) 241.

Fokker-Planck simulations of X3 EC wave absorption experiments in the TCV tokamak

P. Nikkola*, S. Alberti*, S. Coda*, T. P. Goodman*, R. W. Harvey†, E. Nelson-Melby* and O. Sauter*

* *Centre de Recherches en Physique des Plasmas, Association Euratom-Confédération Suisse, Ecole Polytechnique Fédérale de Lausanne, CRPP - EPFL CH-1015 Lausanne*
† *CompX, P.O. Box 2672, Del Mar, CA 92014-5672, USA*

Abstract. Fokker-Planck modeling of the absorption of third harmonic electron cyclotron waves is presented. In the TCV tokamak an advanced electron cyclotron heating system is used to both heat the plasma (ECRH) and drive current (ECCD). Two frequencies are available for heating, 3 MW at 82.7 GHz in X-mode matching the second harmonic of the cyclotron frequency(X2), and 1.5 MW at 117.7GHz which couples to the third harmonic (X3). The X3 waves have a smaller absorption coefficient as the optical thickness of the plasma strongly decreases with the harmonic number. In order to maximize the damping, waves are launched vertically from the top of the vacuum vessel, following the cold X3 resonance. This method alone has been measured to lead to 66% absorption. The Fokker-Planck (F-P) modeling is in agreement with the linear ray tracing code TORAY-GA and both satisfactory reproduce the experimental results.

A second method is based on nonlinear enhancement of the absorption coefficient. A suprathermal electron population with a temperature of about 5 times the bulk temperature is created with the X2 waves. The X3 waves are efficiently damped by this electron population, leading to the measured full absorption of the X3 waves. In this scenario, nonlinear modeling is required, and the F-P calculations are in qualitative agreement with the experiments. However, the simulations suffer from numerical difficulties, and require a large number of mesh points in 3 dimensions (velocity, pitch angle, and radial coordinates). Work is in progress for a better quantitative comparison with the experiment.

INTRODUCTION

One of the main research activities on the TCV tokamak ($R_0 = 0.88\,\mathrm{m}$, $a = 0.25\,\mathrm{m}$, $B_0 = 1.44\,\mathrm{T}$) is the study of Electron Cyclotron Resonance Heating/Current Drive (ECRH/ECCD) in various plasma regimes. ECRH is the only additional heating system with a total of 4.5 MW of Electron Cyclotron (EC) power and the system is constituted of 3.0 MW of 82.7 GHz X-polarized waves at the 2nd EC harmonic (X2), and 1.5 MW of 117.7 GHz waves matching the 3rd harmonic (X3). The power density can be as high as $P_{EC} = 30\,\mathrm{MW/m^3}$, largest in the world in the medium-large size machines. At this high power level, the nonlinear effects on the ECCD have been shown to be important [1,2]. However, the question of nonlinear effects on the wave absorption is less studied because usually the linear codes predict full absorption of X2 waves or O1 in larger tokamaks like ITER.

The situation is different for the X3 waves since the optical thickness of the plasma is a strongly decreasing function of the harmonic number n, $\alpha \sim (k_B T_e / m_e c^2)^{n-1}$. To

increase X3 absorption, the waves are launched vertically approximately parallel to the cold resonance. The absorbed power has been measured to be about 66% in this case [3]. TORAY-GA [4] predicts 43%-75%, depending on the exact launching angle, and similar results are obtained with quasilinear calculations performed by the CQL3D Fokker-Planck (F-P) code [5].

Another way to increase X3 absorption is to create a nonthermal electron population with X2 waves. Since the absorption is effectively proportional to

$$P_{abs} \sim -f\frac{\partial \ln f}{\partial u_{\perp}} \tag{1}$$

where f is the electron distribution function and $u_{\perp}$ is the perpendicular velocity with respect to the magnetic field, increasing f more than decreasing $-\partial \ln f/\partial u_{\perp}$, as compared to a Maxwellian plasma, leads to nonlinear enhancement of P_{abs}, see equation (2). This nonlinearity has been experimentally shown to lead to 100% absorption of X3 waves [6].

VERTICAL LAUNCH OF THE X3 WAVES, LINEAR ABSORPTION

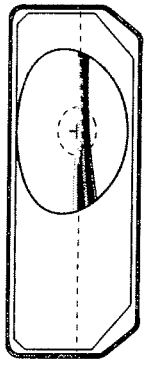

TCV#22877
t=1.7s
$P_{X3} = 0.75MW$
$T_{e,0} = 2keV$
$n_{e0,19} = 5m^{-3}$
$I_p = 230kA$
$V_{loop} = 0.47V$

FIGURE 1. Vertical X3 launching geometry and the key plasma parameters.

The measured X3 absorption in the plasma considered in [3], using the vertical X3 launching geometry, as shown in figure 1, is about 66%. In figure 2a we show the comparison of TORAY-GA calculation with CQL3D results with different velocity meshes. The absorption of CQL3D is in good agreement with the EC wave damping routine of TORAY-GA. In the figure it is also shown that changing the central value of the radial diffusion coefficient, D_0, from 0 to $1\,m^2/s$ or setting the electric field to zero did not affect the damping. The power density profiles of the two codes are almost identical as shown in figure 2b. This calculated absorption of 42-43% is smaller than the observed value. However, the absorbed power is very sensitive to the exact launching angle as shown experimentally and seen with the simulations [3]. In the plasma analyzed in this paper, changing the launcher angle by less than 0.5° increased the TORAY-GA result by a factor of about 2. Thus the difference between the TORAY-GA and CQL3D results and the measured values are within the error bars of the exact launcher aiming and equilibrium reconstruction.

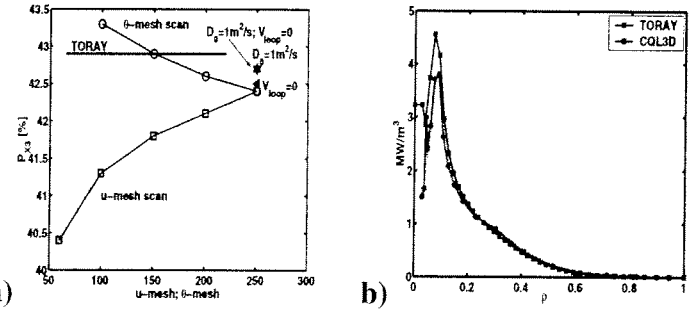

FIGURE 2. a) The CQL3D result is in agreement with the TORAY-GA damping routine. Electric field and radial transport have no effect on the damping. b) Also the power absorption profiles of the two codes agree well.

PREHEATING WITH X2 WAVES, NONLINEAR ABSORPTION

With a finite launching angle between the X2 waves and the normal to the magnetic field, Φ_T^{X2}, a suprathermal electron population is created because the resonance line reaches higher energies than with $\Phi_T^{X2} = 0$ (ECRH). This follows directly from the relativistic EC resonance condition $\omega = \Omega/\gamma + k_{||} v_{||}$.

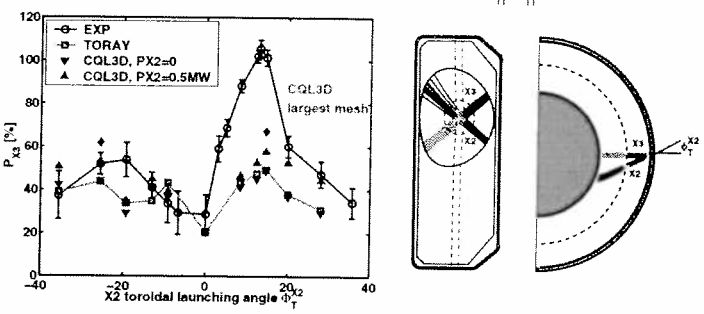

FIGURE 3. The scan of $k_{||}$ of X2 waves and the measured absorption of X3 waves. The simulation results are discussed in the text. The launching geometry is shown on right.

In figure 3 the measured X3 absorption, using the DML signal with X3 modulation, is shown [6]. 100% absorption of X3 waves is observed with an angle of $\Phi_T^{X2} = 15°$ of the X2 waves. In addition, there is an asymmetry between negative (CNT-CD) and positive (CO-CD) launching angles. The assumed reason for the observed synergy in absorption between X2 and X3 waves is that with X2 waves a suprathermal electron population is created if $\Phi_T^{X2} \neq 0$. This population has larger temperature but also f is larger at a high velocity as compared to f_M. Then, according to equation (1), P_{abs} can be higher if

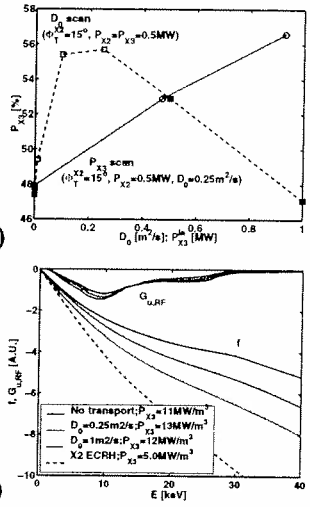

FIGURE 4. a) Effect of transport and X3 power to X3 absorption, b) f and $G_{u,RF}$ with different D_0. Also is shown f with $\Phi_T^{X2} = 0$.

$$f(\mathbf{u}^*) > \frac{\partial_{u_\perp} \ln f_M|_{\mathbf{u}^*}}{\partial_{u_\perp} \ln f|_{\mathbf{u}^*}} f_M(\mathbf{u}^*) \qquad (2)$$

where f_M is the Maxwellian electron distribution function, the X3 wave absorption occurs at the velocity $\mathbf{u}^*$, and $\partial_{u_\perp} \equiv \partial/\partial u_\perp$.

The linear CQL3D results, with zero X2 power (P_{X2}), agree well with TORAY-GA. However, these values are systematically below the observed level. With $P_{X2} = 0.47$MW, implying a non-Maxwellian distribution function, the F-P calculations show an increase in absorption as compared to the linear TORAY-GA results. The absorbed power increases in some cases by up to 30%. Therefore some synergy is also observed in the simulations. However, in CO-CD with Φ_T^{X2} between $5° - 15°$, the experimental absorption still exceeds the calculated one. In figure 3 also the calculation with the largest possible mesh is shown, giving absorption of about 70%. However, the result was not fully converged as the mesh-size is limited by the 3 GB of memory. Thus in order to simulate the strong synergy, a very large mesh is needed. The reason for the asymmetry in figure 3 is not yet known.

This synergy means that part of the X3 power is absorbed in the non-Maxwellian part of the distribution function. Therefore it is interesting to study the effect of transport in

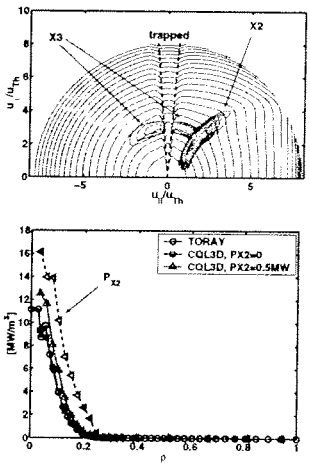

a)

b)

FIGURE 5. a) Quasilinear diffusion coefficients of X2 and X3 waves ($\Phi_T^{X2} = -25°$) and b) comparison of TORAY-GA and CQL3D calculated X3 absorption profiles ($\Phi_T^{X2} = 20°$).

the calculations since with D_0 we can control the suprathermal tail. In figure 4a is shown the absorbed X3 fraction when D_0 is changed from zero (no transport) to $1\,m^2/s$. There is a clear maximum at $D_0 \approx 0.25\,m^2/s$. This is in accordance with equation (2) since without transport f is large at high $\mathbf{u}$ but its logarithmic derivative is reduced as compared to the finite D_0 case. Thus, maximum absorption occurs at a finite D_0. In figure 4b the cuts of f at pitch angle 45° are shown as well as $G_{\mathbf{u}RF} = \mathbf{u}^2\Gamma_{\mathbf{u},RF}$, where $\Gamma_{\mathbf{u},RF} = \mathbf{D}\cdot\partial_{\mathbf{u}}f$ and $\mathbf{D}$ is the quasilinear diffusion tensor. Clearly without transport $-\partial_{u_\perp} \ln f$ is smaller than with $D_0 > 0$ where $G_{u,RF} \neq 0$. With $\Phi_T^{X2} = 0$, f is much smaller than with $\Phi_T^{X2} \neq 0$ and the increase in $-\partial_{u_\perp} \ln f$ can not compensate this. The absorption of X3 is also nonlinear in the X3 input power itself, figure 4a, even though this nonlinearity is lower order. The contours of $G_{\mathbf{u},RF}$ and f are shown in figure 5a. The ECRH resonance of X3 waves and the non-symmetric ECCD resonance of X2 waves overlap and the X2 line reaches to higher energies. The comparison of TORAY-GA and CQL3D calculated absorption profiles is shown in figure 5b for $\Phi_T^{X2} = 20°$. The profiles are almost identical, the CQL3D result with $P_{X2} = 0.5\,MW$ being somewhat broader to account for the difference in total absorbed power. Also the absorption profile of X2 waves is shown.

SUMMARY

The CQL3D Fokker-Planck code is shown to be in accordance with the linear wave damping routine of TORAY-GA for 3rd harmonic heating in very different launching geometries. The enhancement of the absorption due to X2 ECCD is reproduced. The peak absorption is however not fully reproduced by the simulations. This could be due to numerical difficulties, requiring a very large mesh. Work is in progress to improve the convergence.

ACKNOWLEDGMENTS

This work was partly supported by the Swiss National Science Foundation.

REFERENCES

[1] R.W. Harvey *et al,* Phys. Rev. Lett. **88** (2002) 205001.
[2] P. Nikkola *et al,* Submitted to Nuclear Fusion.
[3] S. Alberti *et al,* 29th EPS Conf. on Contr. Fusion and Plasma Phys., Montreux, Switzerland (2002).
[4] K. Matsuda, IEEE Trans. Plasma Sci. PS-17 (1989) 6.
[5] R.W. Harvey and M.G. McCoy, Proc. IAEA TCM/Advances in Simulation and Modeling in Thermonuclear Plasmas, Montreal (1992).
[6] S. Alberti *et al,* Nucl. Fusion **42** (2002) 42.